FULL PAPER

Magnetic Resonance in Medicine

Probing chemical exchange using quantitative spin-lock $R_{1\rho}$ asymmetry imaging with adiabatic RF pulses

Baiyan Jiang[1] | Tao Jin[2] | Thierry Blu[3] | Weitian Chen[1]

[1]Department of Imaging and Interventional Radiology, The Chinese University of Hong Kong, Hong Kong, The Republic of China

[2]Department of Radiology, University of Pittsburgh, Pittsburgh, Pennsylvania

[3]Department of Electrical Engineering, The Chinese University of Hong Kong, Hong Kong, The Republic of China

Correspondence
Weitian Chen, Room 15, Sir Yue Kong Pao Centre for Cancer, Prince of Wales Hospital Shatin, NT Hong Kong, The Republic of China.
Email: wtchen@cuhk.edu.hk

Purpose: CEST is commonly used to probe the effects of chemical exchange. Although $R_{1\rho}$ asymmetry quantification has also been described as a promising option for detecting the effects of chemical exchanges, the existing acquisition approaches are highly susceptible to B_1 RF and B_0 field inhomogeneities. To address this problem, we report a new $R_{1\rho}$ asymmetry imaging approach, AC-iTIP, which is based on the previously reported techniques of irradiation with toggling inversion preparation (iTIP) and adiabatic continuous wave constant amplitude spin-lock RF pulses (ACCSL). We also derived the optimal spin-lock RF pulse B_1 amplitude that yielded the greatest $R_{1\rho}$ asymmetry.

Methods: Bloch-McConnell simulations were used to verify the analytical formula derived for the optimal spin-lock RF pulse B_1 amplitude. The performance of the AC-iTIP approach was compared to that of the iTIP approach based on hard RF pulses and the $R_{1\rho}$-spectrum acquired using adiabatic RF pulses with the conventional fitting method. Comparisons were performed using Bloch-McConnell simulations, phantom, and in vivo experiments at 3.0T.

Results: The analytical prediction of the optimal B_1 was validated. Compared to the other 2 approaches, the AC-iTIP approach was more robust under the influences of B_1 RF and B_0 field inhomogeneities. A linear relationship was observed between the measured $R_{1\rho}$ asymmetry and the metabolite concentration.

Conclusion: The AC-iTIP approach could probe the chemical exchange effect more robustly than the existing $R_{1\rho}$ asymmetry acquisition approaches. Therefore, AC-iTIP is a promising technique for metabolite imaging based on the chemical exchange effect.

KEYWORDS
CEST, spin-lock, $T_{1\rho}$

1 | INTRODUCTION

MRI is among the most widely used imaging modalities in clinical diagnosis. Conventional MRI diagnoses are often based on morphological changes in diseased tissue. In recent years, the mechanism of chemical exchange (CE) contrast has been used to probe diseases at a molecular level and has elicited increasing interest in both clinical and research

settings.[1-10] Generally, CE-based contrast is studied using the chemical exchange saturation transfer.[2,10]

Principally, CEST is based on the effect of saturated proton exchanges between free water and biological molecules. These molecules contain exchangeable protons that resonate at the Larmor frequency, with a chemical shift δ away from that of water. Labile protons can be saturated by applying a selective off-resonance RF pulse. The water signal is then attenuated via the exchange of saturated labile protons and water at CE rate constant, k_{ex}. The normalized water signal intensity can be represented as a function of the RF frequency offset (FO), which is known as the Z-spectrum. The CE signal can be extracted by analyzing asymmetry in the Z-spectrum. The CE rate can usually be divided into 3 regimes: slow ($k_{ex}/\delta \ll 1$), intermediate ($k_{ex}/\delta \sim 1$), and fast exchange ($k_{ex}/\delta \gg 1$). CEST imaging is often performed at slow chemical exchange regime because of the spillover effect caused by direct water saturation.[4]

Spin-lock can also be used to probe the chemical exchange effect.[11-22] This technique can be performed at a range of FOs to extract the chemical exchange contrast related to specific metabolites, and the CE contrast can be calculated based on an asymmetry analysis similar to that used in CEST. These types of approaches are designated as chemical exchange spin-lock (CESL).[11,12] The preparation for CESL magnetization comprises a RF pulse that flips the longitudinal magnetization at a specific flip angle determined by the FO and the frequency of spin-lock (FSL), followed by a spin-lock pulse that locks the spin at that angle. After the spin-lock process, the spins are flipped back to the longitudinal direction by another RF pulse. Compared to CEST, CESL more sensitively detects metabolites at intermediate to fast exchange regimes.[17] However, CESL is significantly hindered by the presence of B_1 RF and B_0 field inhomogeneities, which cause a failure of spin-lock and therefore induce image artifacts and quantification errors. CESL experiments are typically performed at a relatively low FSL.[17] The susceptibility of spin-lock to B_0 field inhomogeneity increases as the FSL decreases. At a low FSL, even a small B_0 field inhomogeneity can result in non-negligible spin-lock errors. The existing methods of artifact correction for constant amplitude spin-lock mostly address on-resonance imaging. Witschey et al[23] reported the compensation of B_1 inhomogeneity during off-resonance spin-lock, using an approach based on the rotary echo method. However, that approach ignored B_0 field inhomogeneity. Other reports suggest that by replacing hard pulses with adiabatic pulses with RF amplitudes matching that of the spin-lock pulse, the spins would be locked along the effective field for both on- and off-resonance spin-lock, even in the presence of B_1 RF and B_0 field inhomogeneities.[22,24,25] This approach should therefore provide artifact-free spin-lock images and $T_{1\rho}$ quantification with simultaneous compensation of B_1 RF and B_0 field inhomogeneities for both on- and off-resonance spin-lock. For convenience, we describe this approach as adiabatic continuous wave constant amplitude spin-lock (ACCSL).

Recently, $R_{1\rho}$ ($1/T_{1\rho}$) asymmetry was described as a promising option for probing metabolites.[15,16] The $R_{1\rho}$ asymmetry signal is free from the effects of water R_1 and R_2 relaxation.[15] The $R_{1\rho}$ asymmetry signal is linearly proportional to the population of the chemical exchanging pool or the concentration of the metabolite of interest.[16] To calculate an $R_{1\rho}$-spectrum, spin-lock images with various time-of-spin-lock (TSL) values can be collected using ACCSL or other spin-lock methods at each FO. Next, the $R_{1\rho}$ can be calculated at each FO by fitting the data to an appropriate relaxation model. For convenience, we term this method the $R_{1\rho}$-fitting approach. The $R_{1\rho}$ can also be obtained using a previously reported approach, irradiation with toggling inversion preparation (iTIP), where an inversion pulse is used to obtain the $R_{1\rho}$ without reaching the steady state.[15] The originally reported iTIP approach was based on a hard RF pulse spin-lock,[15] which is subject to the effects of B_1 RF and B_0 field inhomogeneities. For convenience, we term this approach the hard pulse-based iTIP (HP-iTIP).

In this work, we present a new approach to $R_{1\rho}$ asymmetry imaging for the measurement of metabolites. We use the term AC-iTIP to describe this newly proposed method based on ACCSL with iTIP acquisition. Here, we provide the theory and method by which this AC-iTIP approach can be used to achieve robust $R_{1\rho}$ quantification in the presence of B_1 RF and B_0 field inhomogeneities. We also provide a theoretical derivation of the optimal B_1 of the spin-lock RF pulse required to achieve maximum $R_{1\rho}$ asymmetry for specific metabolites. We further demonstrate the AC-iTIP approach using simulations, phantom, and in vivo experiments.

2 | METHODS

2.1 | Challenges to CESL

The high susceptibility of conventional CESL based on a hard RF pulse spin-lock to B_1 RF and B_0 field inhomogeneities presents a major challenge. However, ACCSL can be used to mitigate this problem. When performing ACCSL, the spins are locked along the effective spin-lock field after adiabatic half passage (AHP) at an angle θ from the longitudinal direction, which is determined by the nominal spin-lock B_1, nominal resonance FO, and B_1 RF and B_0 field inhomogeneities.[24,25] Figure 1A shows the θ values with and without B_0 field inhomogeneity when ACCSL was used at a range of resonance FOs. Note that B_0 field inhomogeneity can result in a discontinuity of θ. Consequently, the CESL Z-spectrum from the ACCSL also exhibits discontinuity, as shown in Figure 1B. In Appendix A,

FIGURE 1 The effect of B_0 field inhomogeneity on the CESL Z-spectrum and the $R_{1\rho}$-spectrum. Spin-lock was performed using ACCSL. (A) The effective spin-lock angle during ACCSL at different resonance FOs. (B) CESL Z-spectrum using ACCSL. and (C) $R_{1\rho}$-spectrum. Blue and red lines indicate the results in the presence and absence of B_0 field inhomogeneity, respectively. Note that the ACCSL Z-spectrum exhibits discontinuity in the presence of B_0 field inhomogeneity, whereas the $R_{1\rho}$-spectrum exhibits a shift equal to B_0 field inhomogeneity
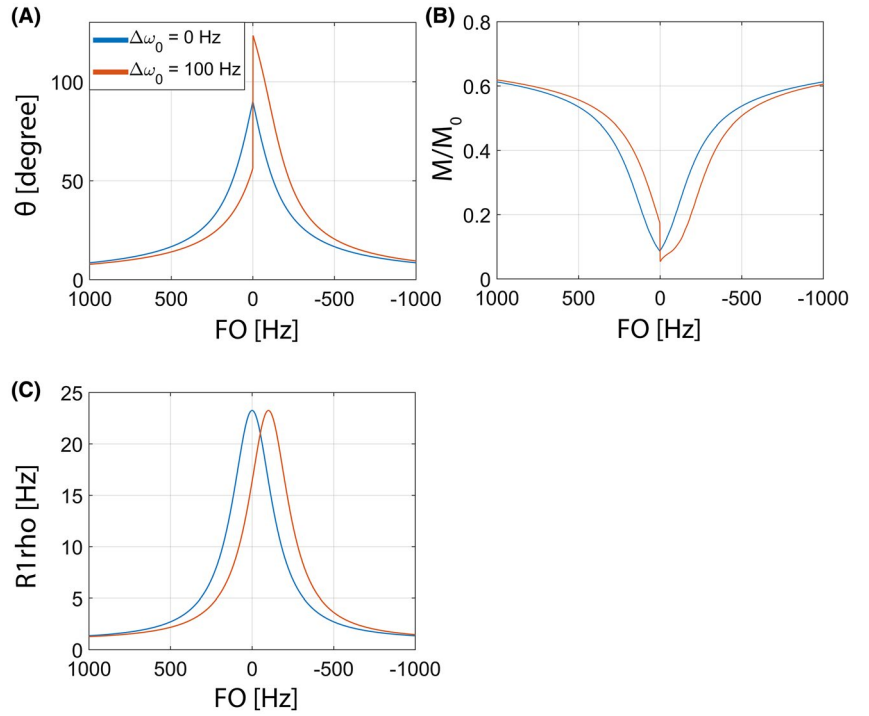
we determine that if the B_0 field inhomogeneity is Δf, the asymmetry analysis of the CESL Z-spectrum acquired using the ACCSL is only valid at FOs outside the range of 0 to $2 \times \Delta f$. This outcome causes 2 problems: (1) the ACCSL cannot detect metabolites with chemical shifts smaller than that of the B_0 field inhomogeneity, and (2) CESL Z-spectrum fitting becomes difficult because of this discontinuity.

These problems can be addressed by calculating the $R_{1\rho}$-spectrum. $R_{1\rho}$ can be approximated as a superposition of 3 terms,[26] namely relaxation because of water (R_{eff}), relaxation because of the CE effect (R_{ex}), and relaxation because of the magnetization transfer (R_{MT}). This approximation can be represented as below

$$R_{1\rho}(FO) = R_1 \cdot \cos^2\theta + (R_2 + R_{ex}) \cdot \sin^2\theta + R_{MT}, \quad (1)$$

where $\cos^2\theta = FO^2 / (w_1^2 + FO^2)$, $\sin^2\theta = w_1^2 / (w_1^2 + FO^2)$, and w_1 denotes the B_1 RF amplitude of the spin-lock RF pulse. As shown in Appendix A, the change in θ at the discontinuity points is $\pm\pi$ in the presence of B_0 field inhomogeneity. As $\sin^2\theta = \sin^2(\theta \pm \pi)$ and $\cos^2\theta = \cos^2(\theta \pm \pi)$, this discontinuity is removed by the squares of the sine and cosine. Therefore, the $R_{1\rho}$-spectrum and associated asymmetry analysis are not affected by the aforementioned problems. Figure 1C depicts $R_{1\rho}$-spectra simulated using ACCSL with and without B_0 field inhomogeneity. Note that B_0 field inhomogeneity, Δf, only caused an equivalent shift in the $R_{1\rho}$-spectrum, rather than discontinuity of the spectrum.

2.2 | Robust $R_{1\rho}$ asymmetry

$R_{1\rho}$ asymmetry can be calculated after using ACCSL to acquire the $R_{1\rho}$ at each resonance FO. However, this approach and the corresponding relaxation model[25] may require a long-duration RF pulse at large FOs to accommodate the prolonged $T_{1\rho}$ at increased FOs. Additionally, during the asymmetry analysis, any small quantification error because of noise can be amplified after the subtraction process. To improve the robustness of the $R_{1\rho}$ quantification, we used the iTIP approach[15] and replaced the hard RF pulse spin-lock in the original iTIP approach with the ACCSL RF pulse cluster. This new approach is termed AC-iTIP. Figure 2 illustrates the spin-lock RF pulse clusters used during AC-iTIP and the original HP-iTIP. Note that the spin-lock RF pulse cluster used in the ACCSL is the same as the pulse cluster used for AC-iTIP but lacked a hard pulse for inversion.[25]

For AC-iTIP, 2 data sets are acquired, one each with the toggling RF pulse turned on and turned off. According to Jiang and Chen,[25] when the toggling RF pulse is turned off, magnetization at the end of the spin-lock RF pulse cluster can be expressed as

$$M^{tsl} = M_{ini1} \cdot e^{-R_{1rho}(FO) \cdot tsl} + C. \quad (2)$$

When the toggling RF pulse is turned on, magnetization at the end of the spin-lock RF pulse cluster can be expressed as

$$M_i^{tsl} = M_{ini2} \cdot e^{-R_{1rho}(FO) \cdot tsl} + C, \quad (3)$$
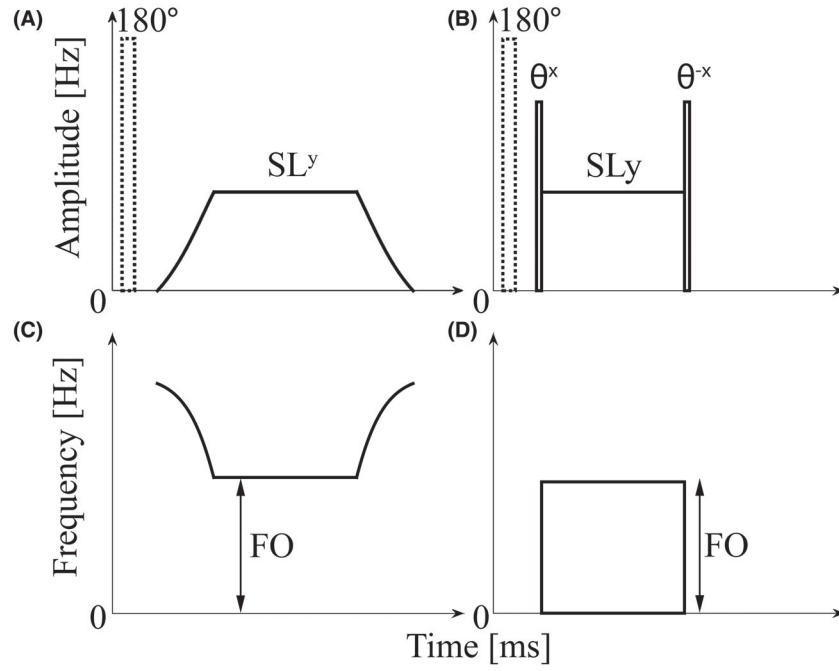
FIGURE 2 The RF pulse waveforms generated using the AC-iTIP approach (A and C) and HP-iTIP approach (B and D). Crushers (not shown) were added between the inversion pulse and spin-lock pulse of both approaches. For the $R_{1\rho}$-fitting approach using ACCSL, the RF pulse waveform was identical to the AC-iTIP RF pulse waveform without the inversion pulse. SL represents the spin-lock pulse. The hard pulse flipped the magnetization to a corresponding effective magnetic field with a flip angle θ

where M_{ini1} and M_{ini2} are the initial magnetizations after the AHP and at the beginning of the spin-lock multiplied by a scaling factor[25]; and C is a term including the contributions from the steady-state magnetization and relaxation effect.[25] Note that the same C term is used in Equations 2 and 3, as this term is calculated using the steady state magnetization, relaxation parameters, and adiabatic waveforms[25] that remain constant regardless of the toggling RF pulse status. Note that M_{ini1} is equal to the negative M_{ini2} determined using the original HP-iTIP when the toggling RF pulse is a perfect 180° pulse. In the AC-iTIP approach, M_{ini1} is not equal to the negative M_{ini2} because of the following reasons: (1) often, the flip angle of the toggling RF pulse is not exactly 180° under the influence of B_1 RF inhomogeneity, particularly if a simple hard pulse is used for the inversion, and (2) the relaxation effect during adiabatic pulses can cause the magnitude of M_{ini1} unequal to that of M_{ini2}, even at a toggling RF pulse flip angle of 180°.

The subtraction of Equation 3 from Equation 2 yields

$$M_t(FO) \equiv M^{tsl} - M_i^{tsl} = (M_{ini1} - M_{ini2}) \cdot e^{-R_{1rho}(FO)\cdot tsl}. \quad (4)$$

Here, $R_{1\rho}$ asymmetry can be calculated by determining the logarithm of $M_t(+FO)/M_t(-FO)$ if the magnitude of $(M_{ini1} - M_{ini2})$ is equal at +FO and –FO.

As demonstrated in Figure 1, the presence of B_0 field inhomogeneity causes discontinuity in the θ spectrum, which can also result in discontinuity of the M_{ini1} and M_{ini2} spectra. Figure 3 demonstrates this effect. In the absence of B_0 field inhomogeneity, M_{ini1} and M_{ini2} are symmetrical with respect to the water frequency, and the magnitude of $(M_{ini1} - M_{ini2})$ is approximately equal at +FO and –FO. In contrast, in the presence of B_0 field inhomogeneity, discontinuities can be observed in the M_{ini1} and M_{ini2} spectra, which leads to unequal $(M_{ini1} - M_{ini2})$ magnitudes at +FO and –FO. To address this problem, data are collected at a TSL of 0 ms to obtain the value $(M_{ini1} - M_{ini2})$. We can combine this with Equation 4 to calculate the $R_{1\rho}$-spectrum and $R_{1\rho}$ asymmetry. If we assume a symmetrical magnetization transfer (MT) effect with respect to the water reference point, then the $R_{1\rho}$ asymmetry can be calculated as

$$R_{1rho,asym} = R_{1rho}(+FO)$$
$$- R_{1rho}(-FO) = \sin^2\theta \cdot (R_{ex}(+FO) - R_{ex}(-FO)). \quad (5)$$

According to Trott and Palmer,[27] R_{ex} for a 2-pool model can be expressed as

$$R_{ex} = \frac{p_b \cdot k \cdot \delta_b^2}{(\delta_b - FO)^2 + w_1^2 + k^2}, \quad (6)$$
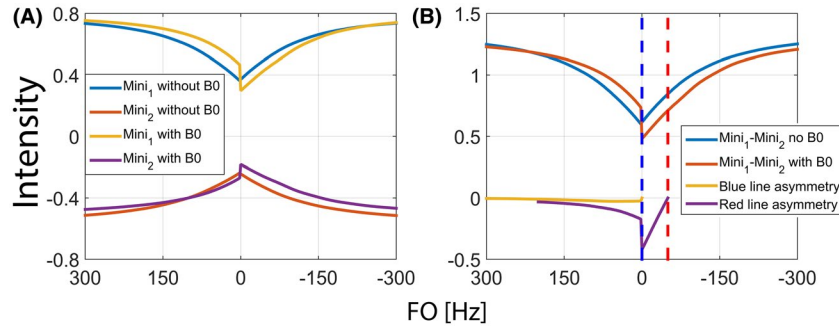
FIGURE 3 Bloch-McConnell simulations of the initial magnetization, M_{ini1} and M_{ini2}, before spin-lock. M_{ini1} and M_{ini2} are defined in Equations 2 and 3. (A) The blue and red solid lines respectively correspond to M_{ini1} and M_{ini2} without B_0 inhomogeneity. The yellow and purple solid lines respectively correspond to M_{ini1} and M_{ini2} with B_0 inhomogeneity. (B) The spectrum and asymmetry of M_{ini1}–M_{ini2} without and with B_0 field inhomogeneity. The symmetrical axis used for the asymmetry calculation is indicated by the dotted lines, which correspond to 0 and -50 Hz in the absence and presence of B_0 field inhomogeneity, respectively. The yellow and purple lines, respectively, correspond to M_{ini1}–M_{ini2} asymmetry in the absence and presence of B_0 field inhomogeneity. Note that in the presence of B_0 field inhomogeneity, the M_{ini1}–M_{ini2} values at $+FO$ and $-FO$ are not equal. Discontinuities are visible on the M_{ini1}, M_{ini2}, and M_{ini1}–M_{ini2} asymmetry spectra

where p_b denotes the population ratio of the labile proton to the water proton, k denotes the CE rate, and δ_b denotes the chemical shift of the metabolite pool.

By substituting Equation 6 into Equation 5, we obtain

$$R_{1rho,asym} = p_b \cdot k \cdot \delta_b^2 \cdot \sin^2\theta \cdot \left(\frac{1}{x_1^2 + w_1^2} - \frac{1}{x_2^2 + w_1^2} \right), \quad (7)$$

where $x_1^2 = (\delta_b + FO)^2 + k^2$ and $x_2^2 = (\delta_b - FO)^2 + k^2$. $R_{1\rho,asym}$ can be acquired selectively for certain groups of labile protons. In contrast, the on-resonance $R_{1\rho}$ receives signal contributions from all labile protons and therefore is not selective for specific metabolites.

2.3 | Optimized B_1 amplitude of the spin-lock RF pulse for $R_{1\rho}$ asymmetry

An optimal saturation RF pulse B_1 amplitude can be used to achieve maximum CEST contrast.[28] During $R_{1\rho}$ asymmetry acquisition, an optimal spin-lock RF pulse B_1 amplitude (or w_1 in Equation 7) also exists and yields the highest $R_{1\rho}$ asymmetry. The optimal spin-lock RF pulse B_1 amplitude can be derived analytically by equating the first derivative of Equation 7 to zero. The optimal w_1 that yields the highest $R_{1\rho}$ asymmetry, denoted as $w_{1,opt}$, can be determined using the following equation (a detailed derivation is provided in Appendix B)

$$\frac{1}{w_{1,opt}^2} = \left(\sqrt{\frac{p^3}{27} + \frac{q^2}{4}} - \frac{q}{2} \right)^{\frac{1}{3}} + \left(-\sqrt{\frac{p^3}{27} + \frac{q^2}{4}} - \frac{q}{2} \right)^{\frac{1}{3}}, \quad (8)$$

where $p = -\left(x_1^2 + x_2^2 + FO^2 \right) / \left(x_1^2 \cdot x_2^2 \cdot FO^2 \right)$ and $q = -2 / \left(x_1^2 \cdot x_2^2 \cdot FO^2 \right)$.

2.4 | Simulation studies

2.4.1 | Simulation study 1: validation of the optimal B_1

We used simulations to demonstrate the existence of the optimal B_1 of the spin-lock RF pulse and validate our analytical derivation. We performed full-equation Bloch-McConnell simulations using both 2-pool and 3-pool models. Detailed pool parameters are presented in the caption to Figure 4. Hyperbolic secant (HS1) pulses were used as the AHP and reverse AHP (rAHP). The pulse parameters were as follows: AHP and rAHP duration, 35 ms; coefficient factor β, 2; and frequency sweep amplitude, 150 Hz. The B_1 amplitudes of the AHP and rAHP equal the applied FSL. We performed 6 simulations using a combination of 2 chemical shifts (1 and 3 ppm) and 3 CE rates (500, 1500, and 3000 s^{-1}). In each experiment, the optimal B_1 determined using the numerical simulation was compared with the optimal B_1 derived using Equation 8.

2.4.2 | Simulation study 2: performance comparison of the AC-iTIP approach with the HP-iTIP in the presence of B_1 RF and B_0 field inhomogeneities

We used 3-pool Bloch-McConnell simulations to demonstrate the improved performance of the AC-iTIP approach relative to the HP-iTIP approach. We compared the $R_{1\rho}$-spectrum determined using AC-iTIP to the iTIP-spectrum obtained using HP-iTIP in the presence of various levels of B_1 RF and B_0 field inhomogeneities. The iTIP-spectrum is defined as the logarithm of Equation 4 divided by $-TSL$. Note that the iTIP-spectrum is a linear function of the $R_{1\rho}$-spectrum according to Equation 4. Simulations were performed using
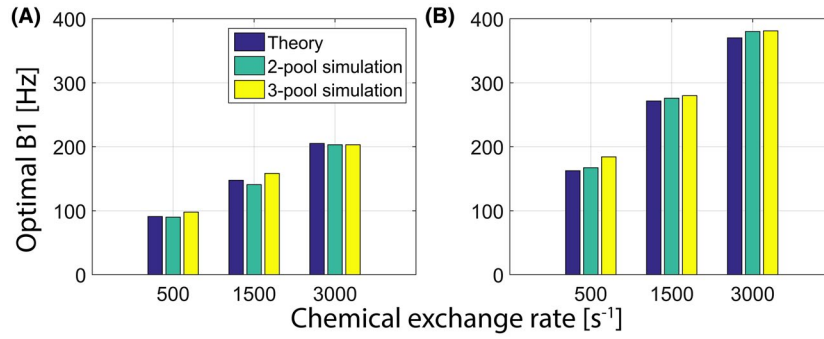
FIGURE 4 Comparison of the theories and Bloch-McConnell simulations used to derive the optimal B_1 amplitude of the spin-lock RF pulse. The following parameters were used for the 2-pool simulation: T_1/T_2 of pool A and B, 1156/43 ms; chemical shift of pool B (metabolite pool), 1 ppm; and chemical exchange rate, 1500 s^{-1}. In the 3-pool model, a third pool representing the magnetization transfer effect was included in the simulation. The magnetization transfer parameters were as follows: T_2, 8.3 μs and magnetization transfer rate, 60 s^{-1}. For the 2-pool model, the water population (p_a) and chemical exchange population (p_b) were 99% and 1%, respectively. For the 3-pool model, the magnetization transfer population (p_c) was 18.2%, the water population (p_a) was 80.8%, and the chemical exchange population (p_b) was 1%. Both 2-pool and 3-pool Bloch-McConnell simulations were performed. The theoretical calculation was based on Equation 8, and the chemical shifts of the exchanging protons with respect to water were (A) 1 and (B) 3 ppm, respectively. Note that our theoretical prediction is consistent with the results of Bloch-McConnell simulations

3 different combinations of B_1 RF and B_0 field inhomogeneities. The parameters of the 3-pool model were identical to those used in the simulation study 1. Unless otherwise stated, TSL 60 ms was used for the HP-iTIP approach, while 0 and 60 ms were used for the AC-iTIP approach. The following additional parameters were applied: FSL = 150, 250, and 300 Hz. FOs were selected from −300 to 300 Hz. Spectra were obtained at 2 different FO intervals, 2 and 25 Hz. Unless otherwise stated, an order of 15 polynomial fittings was used to fit the $R_{1\rho}$-spectrum and iTIP-spectrum for the asymmetry analyses. The $R_{1\rho}$ asymmetry signal was calculated as the mean $R_{1\rho}$ asymmetry value within the range of 1 ± 0.08 ppm.

2.4.3 | Simulation study 3: compare the performance of the AC-iTIP approach to the $R_{1\rho}$-fitting approach based on ACCSL in the presence of noise

Using 3-pool Bloch-McConnell simulations, we compared the performance of the AC-iTIP approach to that of the $R_{1\rho}$-fitting approach based on an ACCSL acquisition at different SNRs. The pool parameters were identical to those used in simulation study 1. FOs of ± 250, ± 200, ± 175, ± 150, ± 125, ± 100, ± 75, ± 50, ± 25, and 0 Hz and a FSL of 150 Hz were used. As the AC-iTIP approach requires 4 acquisitions to measure $R_{1\rho}$ values, 4 TSLs (0, 20, 40, and 60 ms) were used to simulate $R_{1\rho}$-fitting approach data and emulate an equal scan time between the 2 approaches. The $R_{1\rho}$-spectrum determined via the $R_{1\rho}$-fitting approach was obtained by fitting the data to our previously reported relaxation model.[25] Three SNRs were used: 15, 25, and 50. The SNR was calculated as the maximum signal from the acquisition at a FO of 0 Hz and TSL of 0 ms, divided by the SD of noise for both approaches. The added noise adhered to

a zero-mean Gaussian distribution. Simulations without added noise were used as ground truths.

2.5 | Phantom studies

2.5.1 | Phantom study 1: Comparison of the performance of the AC-iTIP approach with the $R_{1\rho}$-fitting approach based on ACCSL in the presence of noise

Imaging data sets were acquired using a Philips Achieva TX 3.0T scanner equipped with dual transmission (Philips Healthcare, Best, the Netherlands). An 8-channel head coil (Invivo, Gainesville, FL) was used as the receiver. Phantoms containing 3% agarose gel were used in this study. 2D fast spin echo (FSE) was used to acquire the imaging data. The FSL, FOs, and TSLs used in the AC-iTIP and $R_{1\rho}$-fitting approaches were identical to those used in simulation study 3. Data were acquired at different levels of SNR and varying TE of 11, 30, and 40 ms. $R_{1\rho}$-spectra obtained using both approaches were compared.

2.5.2 | Phantom study 2: comparison of the performances of the AC-iTIP approach, HP-iTIP approach, and $R_{1\rho}$-fitting approach in the presence of B_1 RF and B_0 field inhomogeneities

In this phantom study, we applied all 3 approaches to 3 phantoms with agarose concentrations of 3% (ROI 1), 4% (ROI 2), and 5% (ROI 3). Phantom data sets were acquired using a 32-channel cardiac coil (Invivo, Gainesville, FL) as the receiver. Scans were performed at FO values of ± 125,

± 100, ± 75, ± 50, and 0 Hz. Data sets were acquired at a FSL of 150 and 300 Hz. In addition to data sets acquired using default shimming, we also acquired data sets using the pencil-beam (PB) shimming over ROI 2 to minimize B_0 field inhomogeneity within the ROI 2. We then compared the $R_{1\rho}$-spectra and iTIP-spectra obtained using the respective approaches.

2.5.3 | Phantom study 3: use of the AC-iTIP approach to measure metabolite concentrations

In this phantom study, we applied the AC-iTIP approach to phantoms containing various concentrations of myo-inositol (0, 20, 30, 50, 100, 150, and 200 mM) dissolved in phosphate-buffered saline (pH = 7.4). The phantoms also included 0.2 mM $MnCl_2$ to modulate both the R_1 and R_2 to ~1.6 and 20 Hz, respectively. The same 8-channel head coil was used as the receiver. Scans were performed over a FO range of −300 to 300 Hz in 25-Hz increments. Data sets were collected at a FSL of 150 and 250 Hz. The experiments were conducted at room temperature.

2.6 | In vivo study

Healthy volunteers underwent in vivo imaging under approval of the institutional review board. The imaging parameters of the in vivo scan included: FOV 16×16 cm^2, single-slice 2D FSE acquisition with a slice thickness of 5 mm, echo train length 27, TR/TE 2000/7.4 ms, and spectral attenuated inversion recovery (SPAIR) for fat suppression. Volunteer imaging experiments were completed using SAR within the Food and Drug Administration limit. Data sets were collected at a FSL of 150 and 250 Hz. For the HP-iTIP and the AC-iTIP approaches, scans were performed over a FO range of −300 to 300 Hz in 25-Hz increments. For the $R_{1\rho}$-fitting approach, scans were performed at FOs of ± 250, ± 200, ± 175, ± 150, ± 125, ± 100, ± 75, ± 50, ± 25, and 0 Hz. For all phantom and in vivo scans, a B_0 field map was collected using a standard dual echo gradient echo acquisition approach with a delta TE of 2 ms. This B_0 map was used to identify the center of the $R_{1\rho}$-spectrum.

3 | RESULTS

Figure 4 compares the analytical optimal B_1 of the spin-lock RF pulse to the optimal B_1 obtained from Bloch-McConnell simulations. Note the consistency between the results. For a fast CE process with a chemical shift of 1 ppm and CE rate of 1500 s^{-1}, the optimal B_1 of the spin-lock RF pulse would be ~150 Hz. This parameter was used in our simulation, phantom, and in vivo experiments.

Figure 5A–L compare the simulated performances of the HP-iTIP and AC-iTIP approaches under B_1 RF and B_0 field inhomogeneities. Both approaches yielded comparable results in the absence of B_1 RF and B_0 field inhomogeneity. However, the $R_{1\rho}$ asymmetry signal decreased with increasing FSL, consistent with our theory. In the presence of field inhomogeneities, the iTIP-spectrum acquired via HP-iTIP exhibits oscillations that can lead to incorrect $R_{1\rho}$ asymmetry. In contrast, when using the AC-iTIP approach, B_0 field inhomogeneity only results in an equal shift of the $R_{1\rho}$-spectrum. More information regarding the performance of both approaches under B_1 RF field inhomogeneity is included in Supporting Information Figure S1.

Figure 6 compares the AC-iTIP and $R_{1\rho}$-fitting approaches under different SNR levels using both simulations and phantom scans. Both approaches yielded similar $R_{1\rho}$-spectra when the SNR was large. However, the $R_{1\rho}$-fitting approach exhibited increasing error as the SNR decreased. In contrast, the AC-iTIP approach could still obtain a reasonable $R_{1\rho}$-spectrum at the same SNR level. In the phantom experiments, noticeable oscillations appeared on the $R_{1\rho}$-spectra at increased TE values when the $R_{1\rho}$-fitting approach was used, and these were attributed to the decreased SNR. In contrast, such oscillations did not occur in the $R_{1\rho}$-spectra obtained using the AC-iTIP approach.

Figure 7 presents the agarose phantom results acquired using the 3 approaches. When PB shimming was not applied, the iTIP-spectra acquired using the HP-iTIP approach contained oscillations. When PB shimming was applied within ROI 2, these distortions became more significant at regions in ROI 1 and ROI 3 because of exacerbated B_0 field inhomogeneity in these regions. The $R_{1\rho}$-fitting approach led to observable oscillations on the $R_{1\rho}$-spectra, which were likely because of noise. In contrast, the AC-iTIP approach yielded reasonable $R_{1\rho}$-spectra under all scenarios, even at ROIs outside the PB shimming region.

Figure 8 presents the metabolite concentrations measured in phantoms using the AC-iTIP approach. Note that the measured $R_{1\rho}$ asymmetry signal exhibits a linear relationship with the metabolite concentration and that the signal decreases as the FSL increases. These findings are consistent with our theoretical prediction of the optimal B_1.

Figures 9 and 10 show the results from in vivo knee scans. Cartilage forms a fairly thin layer, and therefore the SNR is not sufficient for the $R_{1\rho}$-fitting approach. Accordingly a map of cartilage $R_{1\rho}$ asymmetry using the $R_{1\rho}$-fiting approach is not shown. To accommodate the residual fat signal, ROIs were selected on areas of cartilage with minimal fat chemical shift artifacts and minimal fluid, as this would enable a better comparison of the $R_{1\rho}$ asymmetry signals obtained using both approaches. In the muscle regions, the signal averaging within the ROI yielded a sufficient SNR for the $R_{1\rho}$-fitting approach. Therefore, the signal spectra determined using all 3 approaches were compared in the muscle regions. In the cartilage regions, where B_0 field inhomogeneity
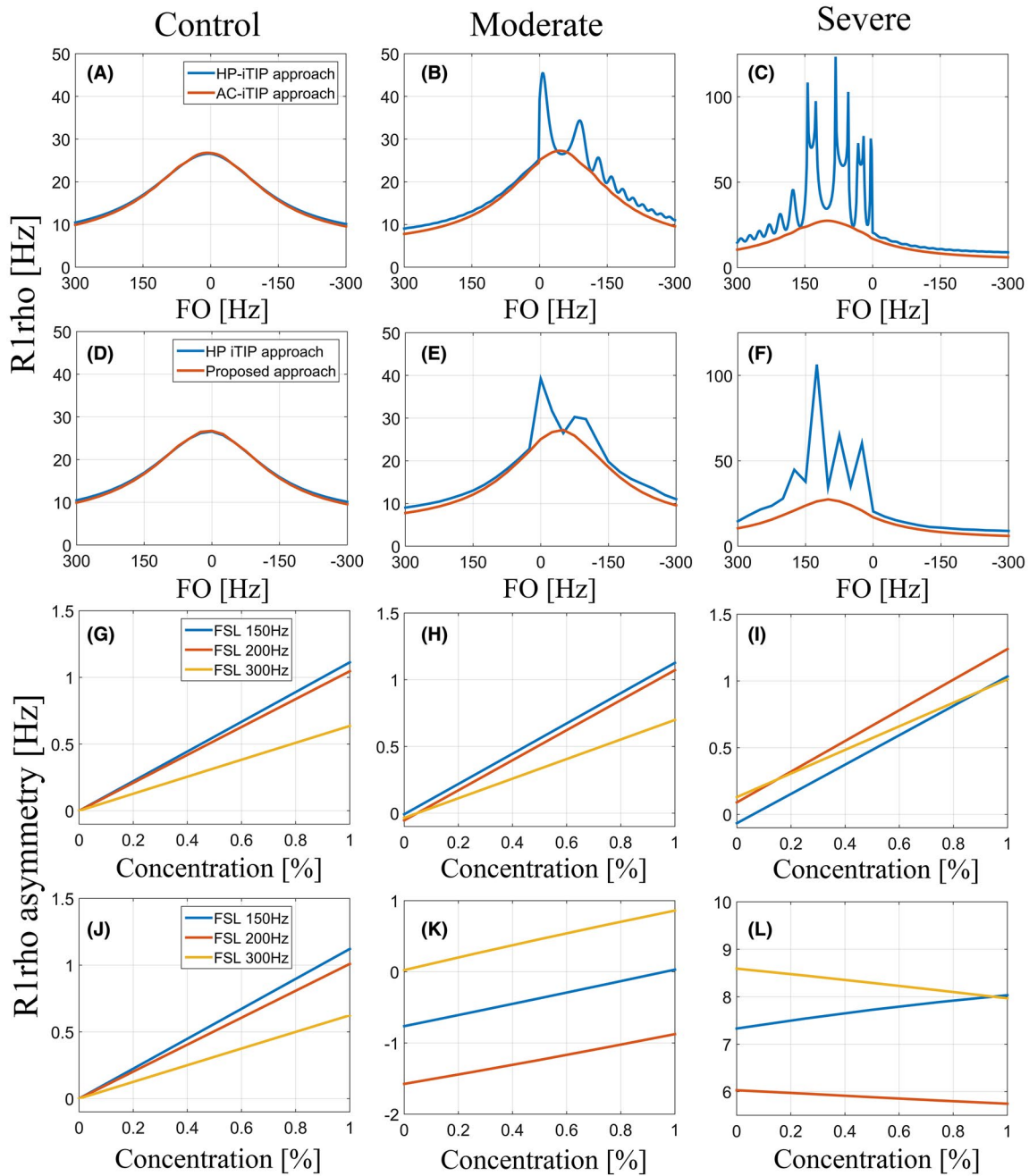
FIGURE 5 The 3-pool Bloch-McConnell simulations of the HP-iTIP and AC-iTIP approaches under 3 levels of field inhomogeneity, including control (no B_1 RF or B_0 field inhomogeneities), moderate (actual B_1 = 90% of the expected B_1 RF amplitude, B_0 field inhomogeneity = 50 Hz), and severe (actual B_1 = 80% of the expected B_1 RF amplitude, B_0 field inhomogeneity = −100 Hz). The top and second rows correspond to FO increments of 2 (A–C) and 25 Hz (D–F), respectively. Blue and red lines represent the spectra generated using the HP-iTIP and AC-iTIP approaches, respectively. The spectra shown in (A)–(F) were simulated using the chemical exchange population, p_b 0.01. The third and fourth rows correspond to $R_{1\rho}$ asymmetry determined using the AC-iTIP (G–I) and HP-iTIP approaches (J–L), respectively. Blue, red, and yellow lines correspond to results derived at a FSL of 150, 200, and 300 Hz, respectively. The results shown in (G)–(L) were simulated using 5 equally spaced p_b concentrations ranging from 0–0.01. The left, middle, and right columns correspond to control (A, D, G, and J), moderate inhomogeneity (B, E, H, and K), and severe inhomogeneity (C, F, I, and L), respectively. Note the oscillations in the iTIP-spectra because of a failure of spin-lock, which also caused errors in $R_{1\rho}$ asymmetry. In contrast, B_0 field inhomogeneity induced a shift equal to field inhomogeneity in the $R_{1\rho}$-spectrum, rather than the oscillation observed when using the AC-iTIP approach. Note that under severe B_1 inhomogeneity, the FSL of 150 Hz is no longer the optimal B_1, and the $R_{1\rho}$ asymmetry signal decreases

was large, the AC-iTIP approach was more robust than the HP-iTIP approach. AC-iTIP and HP-iTIP yielded comparable $R_{1\rho}$ asymmetry signals in the other cartilage regions.

In the muscle regions, the 3 approaches yielded similar results in areas with low B_0 field inhomogeneity. However, the AC-iTIP approach was significantly more robust than the
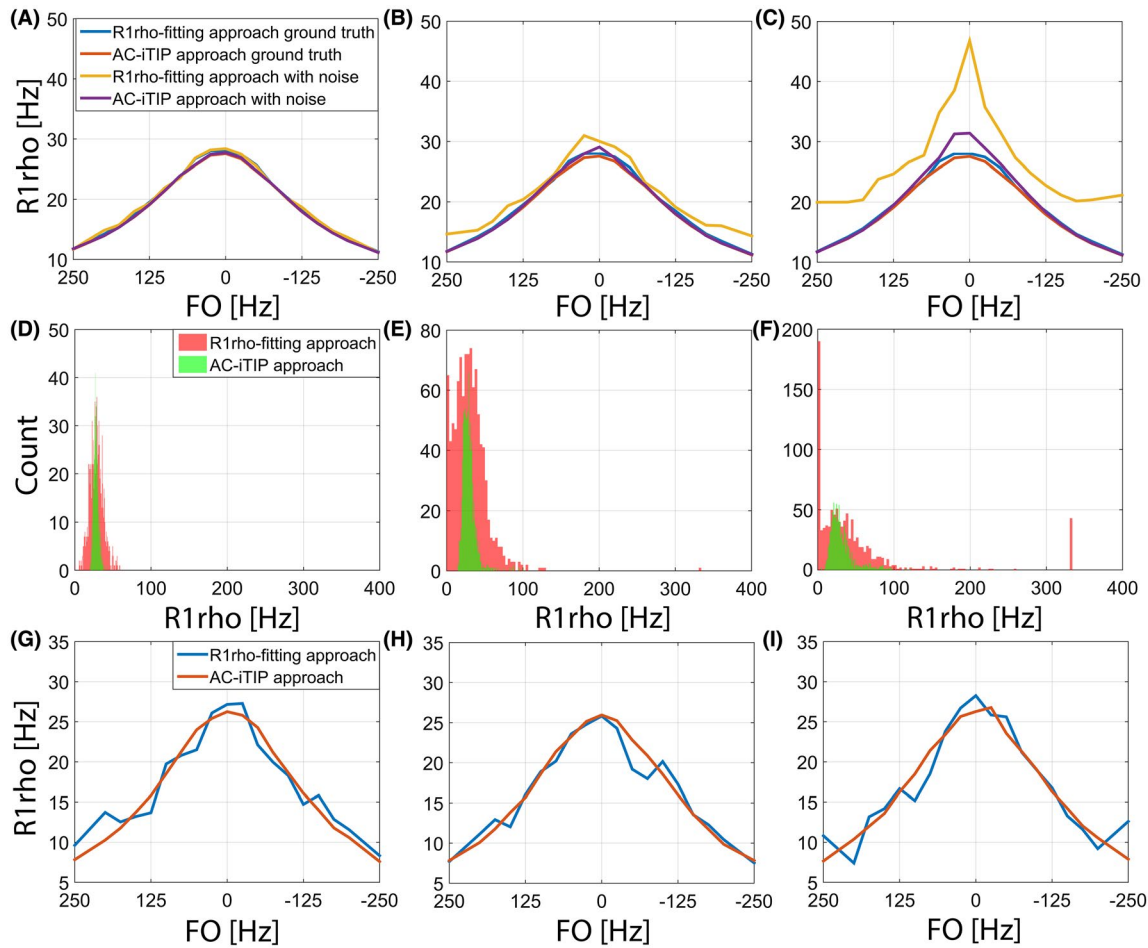
FIGURE 6 Comparison of simulation and phantom results to determine the performances of the AC-iTIP and $R_{1\rho}$-fitting approaches under noise. First row: simulated $R_{1\rho}$-spectrum under SNRs of (A) 50, (B) 25, and (C) 15. Blue and red lines indicate the $R_{1\rho}$-spectra determined using the $R_{1\rho}$-fitting approach and AC-iTIP approach, respectively, in the absence of noise (ground truth). Yellow and purple lines indicate the $R_{1\rho}$-spectra determined using the $R_{1\rho}$-fitting and AC-iTIP approaches, respectively, in the presence of noise. Second row: histograms of simulated on-resonance $R_{1\rho}$ values at SNRs of (D) 50, (E) 25, and (F) 15. Red and green histograms correspond to the results derived using the $R_{1\rho}$-fitting and the AC-iTIP approaches, respectively. Third row: $R_{1\rho}$-spectra obtained from phantom experiments at TE values of (G) 11, (H) 30, and (I) 40 ms, respectively. Blue and red lines indicate the $R_{1\rho}$-spectra derived using the $R_{1\rho}$-fitting and AC-iTIP approaches, respectively. Note that the AC-iTIP approach was more robust under noise, compared to the $R_{1\rho}$-fitting approach. Noticeable oscillation is visible in the $R_{1\rho}$-spectrum obtained using the $R_{1\rho}$-fitting approach, which could lead to errors of $R_{1\rho}$ asymmetry

other 2 approaches in the muscle region characterized by high B_0 field inhomogeneity.

4 | DISCUSSION

Imaging methods based on spin-lock techniques are considered promising approaches for the detection of CE effects. However, these methods are considerably impeded by the strong susceptibility of spin-lock to B_1 RF and B_0 field inhomogeneities. The issue becomes more pronounced when the B_1 amplitudes of spin-lock RF pulses are reduced. B_1 RF and B_0 field inhomogeneities are common occurrences in modern MRI systems. Therefore, the clinical application of spin-lock MRI will require techniques that can address this problem. In

this work, we proposed the AC-iTIP approach as a method for obtaining the $R_{1\rho}$-spectrum and asymmetry in the presence of B_1 RF and B_0 field inhomogeneities. Both our theoretical and experimental analyses demonstrated that this AC-iTIP approach could improve robustness in the presence of system imperfections when compared to existing spin-lock approaches.

The $T_{1\rho}$ dispersion (i.e., dependency of $T_{1\rho}$ on the spin-lock RF amplitude) at the on-resonance spin-lock is sensitive to the CE effect. As the $T_{1\rho}$ dispersion is performed in an on-resonant manner, it is not affected by the direct water saturation effect and could potentially be used to probe intermediate to fast exchange protons. However, $T_{1\rho}$ dispersion is not specific for a certain metabolite. Therefore, $R_{1\rho}$ asymmetry analysis is advantageous because it improves the specificity for target metabolites.
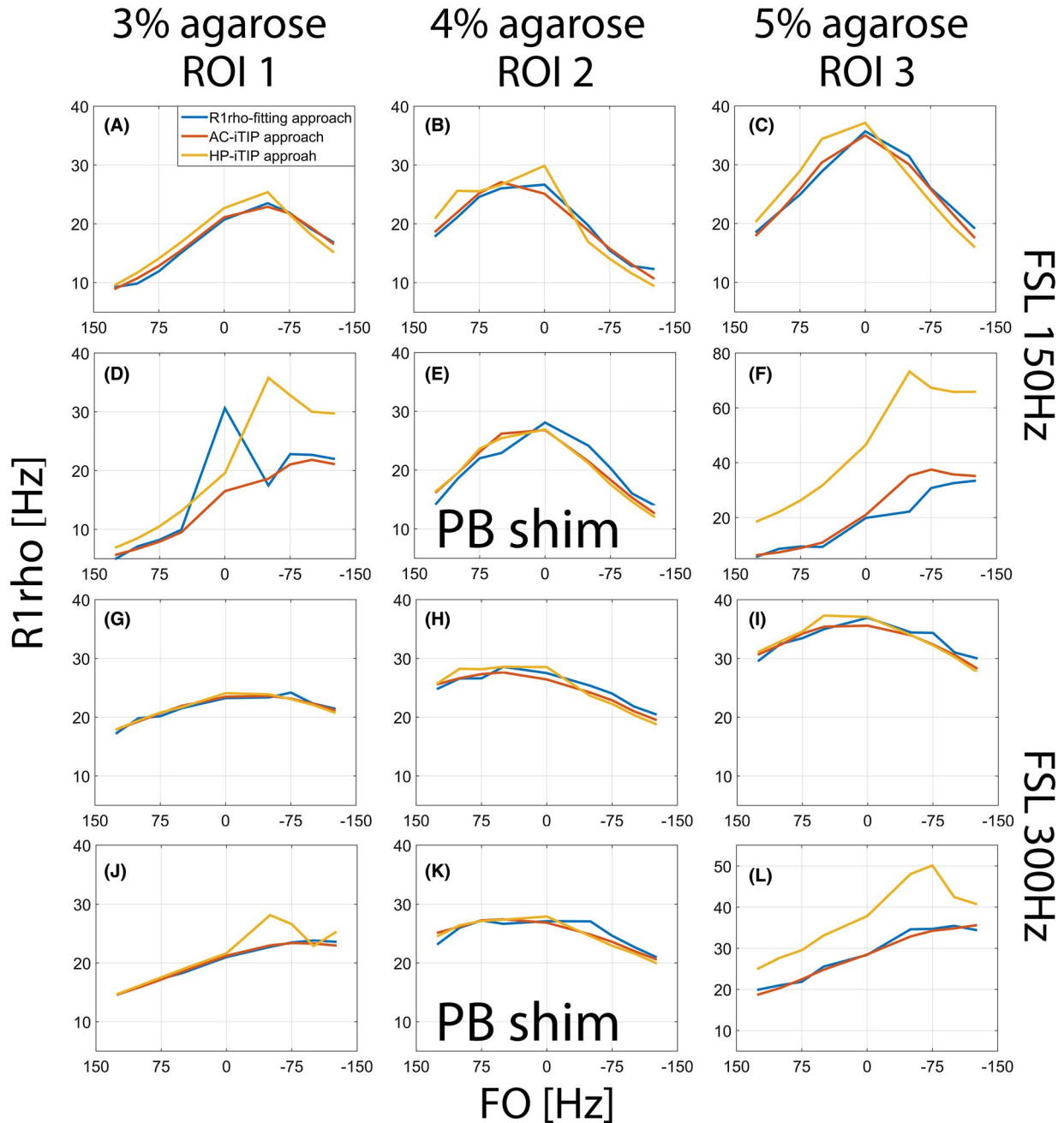
FIGURE 7 Comparison of the performances of the $R_{1\rho}$-fitting, HP-iTIP approach, and AC-iTIP approaches using phantoms containing 3% (ROI 1), 4% (ROI 2), and 5% (ROI 3) agarose. (A–C) and (G–I) $R_{1\rho}$-spectra obtained at a FSL of 150 and 300 Hz, respectively. (D–F) $R_{1\rho}$-spectra obtained using the parameters described in (A)–(C) as well as pencil-beam (PB) shimming applied to ROI 2. (J–L) $R_{1\rho}$-spectra obtained using the same parameters described in (G)–(I), as well as PB shimming applied to ROI 2. PB shimming reduces B_0 field inhomogeneity at ROI 2 but can exacerbate this inhomogeneity at ROI 1 and ROI 3, resulting in oscillations of the iTIP-spectra in those regions. The $R_{1\rho}$-spectra obtained using the $R_{1\rho}$-fitting approach exhibited oscillations that were likely because of increased sensitivity to noise. Compared to the other 2 approaches, the AC-iTIP approach yielded a more robust $R_{1\rho}$-spectrum in the presence of B_0 field inhomogeneity

We further performed 5-pool Bloch-McConnell simulations using multiple CE pools and have provided the simulation parameters and results in Supporting Information Figure S2. Notably, the HP-iTIP and AC-iTIP approaches yielded nearly identical $R_{1\rho}$ asymmetries. The inclusion of additional chemical shift pools in the 5-pool model and the consequent broadening of $R_{1\rho}$ asymmetry led to a shift of the $R_{1\rho}$ asymmetry signal when compared to that of the 3-pool model. However, the additional pools did not affect the linear relationship between $R_{1\rho}$ asymmetry and the concentration
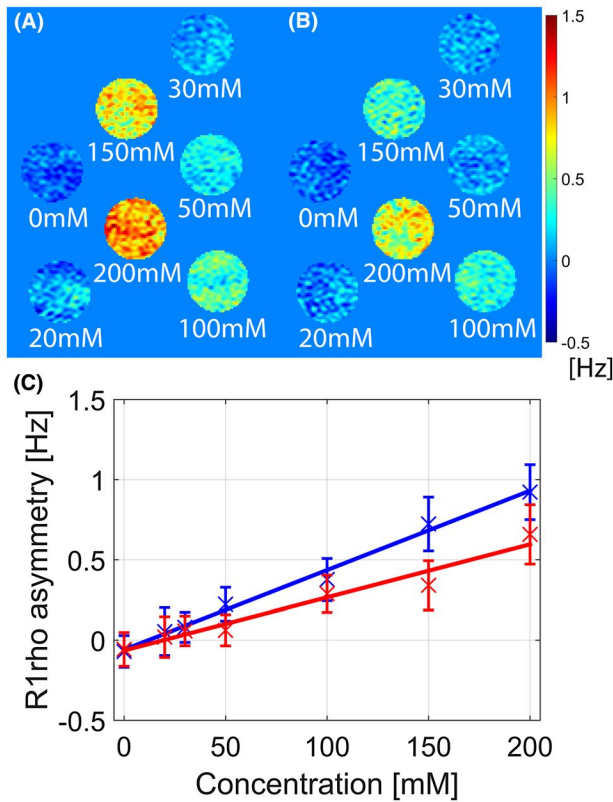
FIGURE 8 AC-iTIP analysis of phantoms containing various concentrations of myo-inositol. (A) Quantitative $R_{1\rho}$ asymmetry map acquired at a FSL of 150 Hz. (B) Quantitative $R_{1\rho}$ asymmetry map acquired at a FSL of 250 Hz. (C) Line plots of the averaged $R_{1\rho}$ asymmetry within each ROI versus the myo-inositol concentration at different FSLs. The error bars represent the SDs, while blue and red lines correspond to a FSL of 150 and 250 Hz, respectively. Note the presence of a linear relationship between $R_{1\rho}$ asymmetry and the metabolite concentration. Moreover, $R_{1\rho}$ asymmetry decreases with increasing FSL, consistent with our theory

of the specified metabolite. These simulation studies indicate that the HP-iTIP and AC-iTIP exhibit comparable specificity for metabolites.

We additionally derived an analytical expression of the optimal B_1, the calculation of which requires prior knowledge of the exchange rate. For a chemical shift of 1 ppm at 3.0T, the optimal B_1 would range from ~120–170 Hz at exchange rates of 1000–2000 s^{-1}. Because we do not know the exact exchange rate, the calculated optimal B_1 may only estimate the actual optimal B_1. Nevertheless, the theory of an optimal B_1 can be used to guide the selection of the spin-lock RF amplitude during $R_{1\rho}$ asymmetry imaging. Moreover, the formula derived for the optimal B_1 may be used to derive the exchange rate from the observed maximum $R_{1\rho}$ asymmetry.

The AC-iTIP approach requires the additional acquisition of data at a TSL of 0 ms, which provides information to generate a full $R_{1\rho}$-spectrum. However, this additional acquisition increases the scan time. When using the HP-iTIP approach, a signal average may be needed for data acquired at a non-zero TSL. Images acquired with a TSL of 0 ms typically have a much higher SNR than images with non-zero TSLs, which may not require signal averaging. Data acquired using the AC-iTIP provided redundant information along both the TSL and frequency dimension. Advanced image reconstruction methods could potentially use this data redundancy and therefore reduce the AC-iTIP scan times.

Note that the AC-iTIP approach requires an adiabatic condition. In our experiments, we used hyperbolic secant (HS1) pulses for the AHP and reverse AHP, with a relatively long duration of 35 ms at a FSL 150 Hz. Other adiabatic RF pulse designs have been reported for the spin-lock.[22] It becomes increasingly difficult to satisfy the adiabatic condition at lower FSL values. The AC-iTIP approach would benefit from the
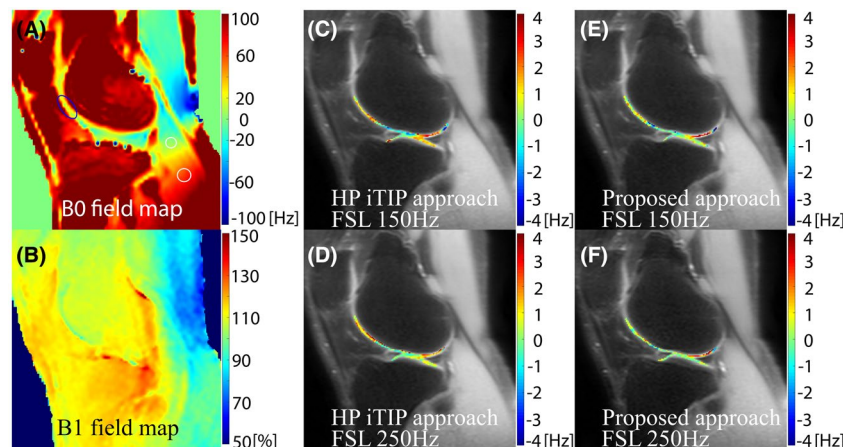
FIGURE 9 Maps of $R_{1\rho}$ asymmetry from in vivo knee images, obtained using the HP-iTIP and AC-iTIP approaches. (A) B_0 field map (in Hz). (B) B_1 field map (in unit percentages; 100% = no B_1 inhomogeneity). (C and D) $R_{1\rho}$ asymmetry maps obtained using the HP-iTIP approach at FSL values of 150 and 250 Hz, respectively. (E and F) $R_{1\rho}$ asymmetry maps obtained using the AC-iTIP approach at FSL values of 150 and 250 Hz, respectively. $R_{1\rho}$ asymmetry maps are overlaid on anatomic maps
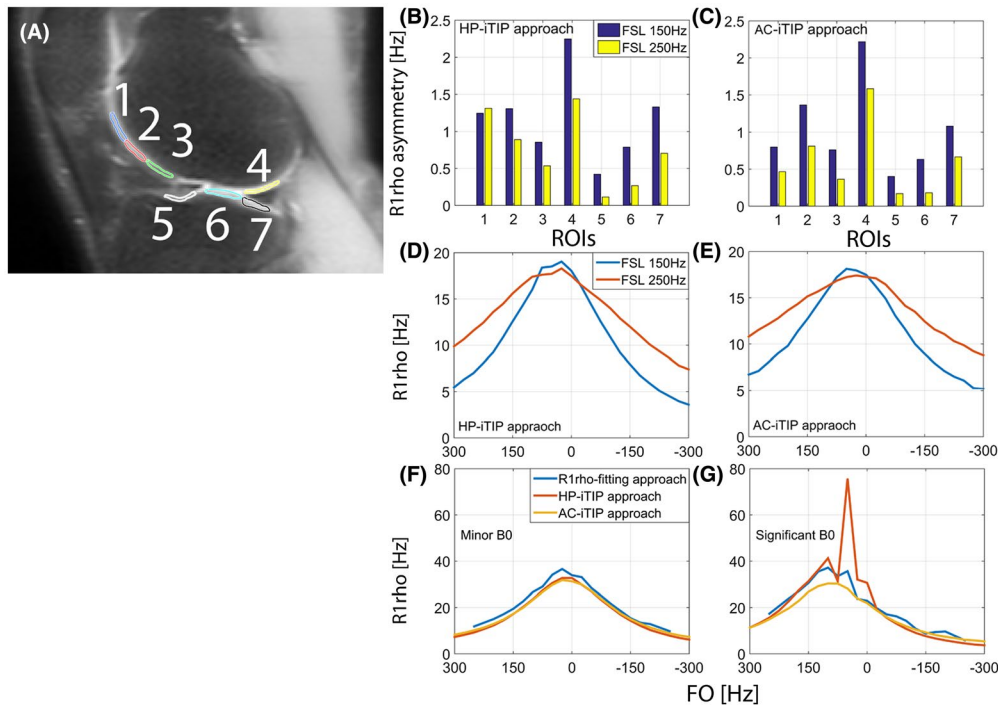
FIGURE 10 Comparison of the HP-iTIP and AC-iTIP approaches when applied to in vivo knee scan data. When using the AC-iTIP approach, a clear residual fat signal was observed when the toggling RF was switched on, with a fat shift direction toward the feet. The readout bandwidth was selected as the maximum water-fat shift for the purpose of the SNR. Seven ROIs that excluded chemical shift artifacts and obvious fluid signals were selected, as indicated in (A). (B and C) Regional average $R_{1\rho}$ asymmetry values within the ROIs at FSL values of 150 (blue bars) and 250 Hz (yellow bars) determined using the HP-iTIP and AC-iTIP approaches, respectively. Note that for the HP-iTIP approach, $R_{1\rho}$ asymmetry in ROI 1 did not decrease as the FSL increased, likely because of the presence of larger B_0 field inhomogeneity (blue circle in Figure 9A). (D and E) Spectra at ROI 1 obtained using the HP-iTIP and AC-iTIP approaches, respectively. Note that the iTIP-spectrum at FSL values of 150 and 250 Hz is clearly distorted at a FO of ~50 Hz. In contrast, the AC-iTIP approach was not affected by B_0 field inhomogeneity. (F and G) Respective spectra obtained at 2 muscle ROIs (the 2 white circles in Figure 9A) using the $R_{1\rho}$-fitting, HP-iTIP, and AC-iTIP approaches at a FSL of 150 Hz. All 3 approaches yielded similar spectra at the muscle region with minor B_0 field inhomogeneity. However, visible distortions appeared on the iTIP-spectrum at the region with large B_0 field inhomogeneity. Moreover, the $R_{1\rho}$-spectrum derived using the $R_{1\rho}$-fitting approach exhibits oscillations that are likely because of noise. The AC-iTIP approach was more robust than the other 2 approaches

development of adiabatic RF pulses that could satisfy the adiabatic condition together with an optimized RF pulse duration at a low FSL.

In our $R_{1\rho}$ asymmetry derivation, we assumed a symmetrical MT effect with respect to the water reference point. However, other reports indicate that MT exhibits a chemical shift away from the water reference point in vivo.[29,30] This effect on $R_{1\rho}$ asymmetry should be investigated in future studies.

In our in vivo studies, we noticed that the SPAIR fat suppression method used in our pulse sequence did not provide sufficient fat suppression for the proposed AC-iTIP approach when the toggling RF pulse was turned on, leading to noticeable chemical shift artifacts. This chemical shift effect decreased the reliability of $R_{1\rho}$ asymmetry at the bone–cartilage interfaces. This problem may be addressed using alternative pulse sequence design, which will be discussed in our future work.

The repeatability and reproducibility of an imaging technique must be determined before its application in clinical

practice. Accordingly, the AC-iTIP approach relies on the determination of the correct field map, which is then used to calculate $R_{1\rho}$ asymmetry accurately. In our studies, we acquired a field map using the standard dual echo gradient echo acquisition method, although the map could also be obtained using the $R_{1\rho}$-spectrum itself or the WASSR[31] approach. Further studies are needed to evaluate the method used to obtain the field map and the repeatability and reproducibility of the AC-iTIP approach. The preliminary repeatability and reproducibility are shown in Supporting Information Figures S3 and S4.

5 | CONCLUSION

Here, we propose the AC-iTIP approach to improve the robustness of $R_{1\rho}$-spectrum and asymmetry measurements. Using simulation, phantom, and in vivo studies, we demonstrate that this approach achieves better performance than that of other spin-lock approaches in terms of calculating

$R_{1\rho}$-spectrum and asymmetry, which can be used to probe the CE effect.

ACKNOWLEDGMENTS

ORCID

Tao Jin https://orcid.org/0000-0003-2912-3517

Weitian Chen https://orcid.org/0000-0001-7242-9285

REFERENCES

1. Liepinsh E, Otting G. Proton exchange rates from amino acid side chains - implications for image contrast. *Magn Reson Med*. 1996;35:30-42.
2. Ward K, Aletras A, Balaban R. A new class of contrast agents for MRI Based on proton chemical exchange dependent saturation transfer (CEST). *J Magn Reson*. 2000;143:79-87.
3. Zhou J, Payen JF, Wilson DA, Traystman RJ, van Zijl PC. Using the amide proton signals of intracellular proteins and peptides to detect pH effects in MRI. *Nat Med*. 2003;9:1085-1090.
4. Zhou J, van Zijl PC. Chemical exchange saturation transfer imaging and spectroscopy. *Prog Nucl Magn Reson Spectrosc*. 2006;48:109-136.
5. Sun PZ, Zhou J, Sun W, Huang J, van Zijl PC. Detection of the ischemic penumbra using pH-weighted MRI. *J Cereb Blood Flow Metab*. 2006;27:1129-1136.
6. Vinogradov E, He H, Lubag A, Balschi JA, Sherry AD, Lenkinski RE. MRI detection of paramagnetic chemical exchange effects in mice kidneys in vivo. *Magn Reson Med*. 2007;58:650-655.
7. Zhou J, Blakeley JO, Hua J, et al. Practical data acquisition method for human brain tumor amide proton transfer (APT) imaging. *Magn Reson Med*. 2008;60:842-849.
8. Zhou J, Tryggestad E, Wen Z, et al. Differentiation between glioma and radiation necrosis using molecular magnetic resonance imaging of endogenous proteins and peptides. *Nat Med*. 2010;17:130-134.
9. Jia G, Abaza R, Williams JD, et al. Amide proton transfer MR imaging of prostate cancer: a preliminary study. *J Magn Reson Imaging*. 2011;33:647-654.
10. van Zijl PC, Yadav NN. Chemical exchange saturation transfer (CEST): what is in a name and what isn't? *Magn Reson Med*. 2011;65:927-948.
11. Jin T, Autio J, Obata T, Kim SG. Spin-locking versus chemical exchange saturation transfer MRI for investigating chemical exchange process between water and labile metabolite protons. *Magn Reson Med*. 2010;65:1448-1460.
12. Yuan J, Zhou J, Ahuja AT, Wang Y. MR chemical exchange imaging with spin-lock technique (CESL): a theoretical analysis of the Z-spectrum using a two-poolR1ρrelaxation model beyond the fast-exchange limit. *Phys Med Biol*. 2012;57:8185-8200.
13. Jin T, Wang P, Zong X, Kim SG. Magnetic resonance imaging of the amine-proton EXchange (APEX) dependent contrast. *NeuroImage*. 2012;59:1218-1227.
14. Zaiss M, Bachert P. Exchange-dependent relaxation in the rotating frame for slow and intermediate exchange - modeling off-resonant spin-lock and chemical exchange saturation transfer. *NMR Biomed*. 2012;26:507-518.
15. Jin T, Kim SG. Quantitative chemical exchange sensitive MRI using irradiation with toggling inversion preparation. *Magn Reson Med*. 2012;68:1056-1064.
16. Ling W, Nicholls FJ, Jin T, et al. Selective detection of chemical exchange specific R1rho by iTIP gagCEST. In Proceedings of the 23rd Annual Meeting of ISMRM, Milan, Italy, 2014. p. 3324.
17. Jin T, Kim SG. Advantages of chemical exchange-sensitive spin-lock (CESL) over chemical exchange saturation transfer (CEST) for hydroxyl- and amine-water proton exchange studies. *NMR Biomed*. 2014;27:1313-1324.
18. Wang P, Block J, Gore JC. Chemical exchange in knee cartilage assessed by R1ρ (1/T1ρ) dispersion at 3T. *Magn Reson Imaging*. 2015;33:38-42.
19. Schuenke P, Koehler C, Korzowski A, et al. Adiabatically prepared spin-lock approach for T1ρ-based dynamic glucose enhanced MRI at ultrahigh fields. *Magn Reson Med*. 2016;78:215-225.
20. Zu Z, Li H, Jiang X, Gore JC. Spin-lock imaging of exogenous exchange-based contrast agents to assess tissue pH. *Magn Reson Med*. 2017;79:298-305.
21. Zu Z, Jiang X, Xu J, Gore JC. Spin-lock imaging of 3-o-methyl-D glucose (3oMG) in brain tumors. *Magn Reson Med*. 2018;80:1110-1117.
22. Herz K, Gandhi C, Schuppert M, Deshmane A, Scheffler K, Zaiss M. CEST imaging at 9.4 T using adjusted adiabatic spin-lock pulses for on- and off-resonant T1ρ-dominated Z-spectrum acquisition. *Magn Reson Med*. 2018;81:275-290.
23. Witschey WRT, Borthakur A, Elliott MA, et al. Compensation for spin-lock artifacts using an off-resonance rotary echo in T1ρ off-weighted imaging. *Magn Reson Med*. 2006;57:2-7.
24. Chen W. Artifacts correction for T1rho imaging with constant amplitude spin-lock. *J Magn Reson*. 2017;274:13-23.
25. Jiang B, Chen W. On-resonance and off-resonance continuous wave constant amplitude spin-lock and T1ρ quantification in the presence of B1 and B0 inhomogeneities. *NMR Biomed*. 2018;31:e3928.
26. Zaiss M, Zu Z, Xu J, et al. A combined analytical solution for chemical exchange saturation transfer and semi-solid magnetization transfer. *NMR Biomed*. 2015;28:217-230.
27. Trott O, Palmer AG. R1ρ Relaxation outside of the fast-exchange limit. *J Magn Reson*. 2002;154:157-160.
28. Sun PZ, van Zijl PC, Zhou J. Optimization of the irradiation power in chemical exchange dependent saturation transfer experiments. *J Magn Reson*. 2005;175:193-200.
29. Hua J, Jones CK, Blakeley J, Smith SA, van Zijl PC, Zhou J. Quantitative description of the asymmetry in magnetization transfer effects around the water resonance in the human brain. *Magn Reson Med*. 2007;58:786-793.
30. Malyarenko DI, Zimmermann EM, Adler J, Swanson SD. Magnetization transfer in lamellar liquid crystals. *Magn Reson Med*. 2013;72:1427-1434.

31. Kim M, Gillen J, Landman BA, Zhou J, van Zijl PC. Water saturation shift referencing (WASSR) for chemical exchange saturation transfer (CEST) experiments. *Magn Reson Med*. 2009;61:1441-1450.

SUPPORTING INFORMATION

Additional supporting information may be found online in the Supporting Information section at the end of the article.

FIGURE S1 The robustness of HP-iTIP and AC-iTIP in terms of B_1 field inhomogeneity. We repeated the chemical exchange phantom experiment described in the manuscript with a large FOV and a lack of RF shimming from the dual transmitter, which resulted in elevated B_1 RF inhomogeneity within the FOV. To avoid the confounding effects of B_0 field inhomogeneity, we drew ROIs at regions with obvious B_1 inhomogeneity and negligible B_0 field inhomogeneity. The 2 regions have ~80% B_1 inhomogeneity (100% = no B_1 inhomogeneity) and a $B_0 \leq |5|$ Hz. The oscillations on spectra derived using the original HP-iTIP approach are because of the presence of B_1 inhomogeneity. In contrast, no oscillation is observed on $R_{1\rho}$-spectra obtained using the AC-iTIP approach. These data illustrate the increased robustness of the AC-iTIP approach versus the HP-iTIP approach in the presence of B_1 RF inhomogeneity

FIGURE S2 Full-equation Bloch-McConnell simulations of the CESL spectrum and asymmetry based on the conventional hard RF pulse spin-lock and ACCSL with (A) a 3-pool model and (B) 5-pool model. Full-equation Bloch-McConnell simulations of the $R_{1\rho}$-spectrum and asymmetry generated using the HP-iTIP and AC-iTIP approaches with (C) a 3-pool model and (D) 5-pool model. (E) Simulation of the $R_{1\rho}$ asymmetry signal as a function of the chemical exchange pool population (p_b). No B_1 RF and B_0 field inhomogeneities were included in the simulations. For (A)–(D), the simulations were performed using 1001 equally spaced FOs ranging from -1000 to 1000 Hz; a FSL of 150 Hz; TSLs of 60 ms for conventional spin-lock and ACCSL, 0 and 60 ms for the AC-iTIP approach; and 60 ms for the HP-iTIP approach; and adiabatic pulse durations of 35 and 70 ms. The parameters of the 3-pool model were identical to those used in simulation study 1. Two extra chemical change pools with chemical shifts of 3 and 5 ppm, pool populations of 0.01, and chemical exchange rates of 500 s^{-1} were added to the 5-pool model. For this model, the water pool population was changed to 0.788. Note the HP-iTIP and the AC-iTIP yielded similar $R_{1\rho}$-spectrum and nearly identical $R_{1\rho}$ asymmetry when either model was used. For the AC-iTIP, increases in the durations of the AHP and rAHP from 35 to 70 ms did not appear to affect the $R_{1\rho}$ asymmetry signal. In the 5-pool model, a signal peak at ~1 ppm, which corresponded to the chemical exchange pool, can be observed on the $R_{1\rho}$ asymmetry signal but absent from the CESL asymmetry signal.

Eleven equally spaced chemical exchange pool populations, p_b, from 0–0.01 were used to derive the simulation results shown in (E). The HP-iTIP and AC-iTIP approaches yielded comparable $R_{1\rho}$ asymmetry signals as functions of the p_b population. The additional chemical shift pools in the 5-pool model broadened the $R_{1\rho}$ asymmetry and therefore caused a shift in the asymmetry signal relative to that obtained using the 3-pool model. However, this shift did not affect the linear relationship between $R_{1\rho}$ asymmetry and the specified metabolite concentration

FIGURE S3 $R_{1\rho}$ asymmetry maps generated from in vivo scans of a healthy volunteer to evaluate repeatability and reproducibility of the proposed AC-iTIP. In this experiment, the volunteer underwent a baseline exam on the first day and a repeated exam on the second day to test the reproducibility. The volunteer received 2 repeated scans within each exam to test the repeatability. The scans were performed using a Philips 3.0T human scanner. The other parameters and set-up were identical to those described for corresponding experiments in the manuscript

FIGURE S4 Another study to evaluate repeatability and reproducibility of the proposed AC-iTIP. In this experiment, the volunteer underwent a baseline exam at noon and a repeated exam in the evening of the same day to test the reproducibility. The volunteer received 2 repeated scans within each exam to test the repeatability. The scans were performed using a Philips 3.0T human scanner. The other parameters and set-ups were identical to those described for corresponding experiments in the manuscript

APPENDIX A

As shown in our previous work,[25] the ACCSL can ensure the spins are effectively locked throughout the spin-lock process at an angle

$$
\theta(r) = \begin{cases}
\tan^{-1}\left(\frac{\tilde{\omega}_{sl}(r)}{\Delta\omega_c + \Delta\omega_0(r)}\right) + \pi, & \text{if } \Delta\omega_c > 0 \text{ and } \Delta\omega_c + \Delta\omega_0(r) \leq 0 \\
\tan^{-1}\left(\frac{\tilde{\omega}_{sl}(r)}{\Delta\omega_c + \Delta\omega_0(r)}\right) - \pi, & \text{if } \Delta\omega_c < 0 \text{ and } \Delta\omega_c + \Delta\omega_0(r) \geq 0 \\
\tan^{-1}\left(\frac{\tilde{\omega}_{sl}(r)}{\Delta\omega_c + \Delta\omega_0(r)}\right), & \text{otherwise}
\end{cases}
$$

(A1)

where $\theta(r)$ represents the angle between the magnetization and the z-axis, r is the spatial location, $\Delta\omega_c$ is the resonant FO of the spin-lock RF pulse, $\Delta\omega_0(r)$ is the B_0 field

inhomogeneity, and $\tilde{\omega}_{sl}(r)$ is the actual spin-lock B_1 amplitude, which is the expected spin-lock amplitude under the influence of B_1 RF inhomogeneity. The discontinuity of θ occurs at $\Delta\omega_c = 0$, and $\Delta\omega_c + \Delta\omega_0(r) = 0$. This is because of the fact that the magnetization and the effective spin-lock field can be either parallel or anti-parallel with each other, depending on the FO of spin-lock and the B_0 field inhomogeneity. Consequently, the asymmetry analysis of the CESL Z-spectrum acquired using the ACCSL is only valid at FO outsides the range of 0 to $2\Delta\omega_0(r)$, and the ACCSL is unable to detect metabolites with chemical shift smaller than that of the B_0 field inhomogeneity.

APPENDIX B

Starting from Equation 7, if we define w_1^2 as x, and f(x) as the $R_{1\rho}$ asymmetry, it can be written as

$$f(x) = A \cdot \frac{x}{x + FO^2} \cdot \left(\frac{1}{x + x_1^2} - \frac{1}{x + x_2^2} \right), \quad (B1)$$

where $A = pb \cdot k \cdot \delta_b^2$, $x_1^2 = (\delta_b + FO)^2 + k^2$, and $x_2^2 = (\delta_b - FO)^2 + k^2$. Rearranging terms, we get

$$f(x) = a1 \cdot \frac{x}{(x + FO^2) \cdot (x + x_1^2) \cdot (x + x_2^2)}, \quad (B2)$$

where $a1 = A \cdot (x_2^2 - x_1^2)$. The first derivative of f(x) equals to zero can be written as

$$f'(x) = \frac{1}{x} - \frac{1}{(x + FO^2)} - \frac{1}{(x + x_1^2)} - \frac{1}{(x + x_2^2)} = 0, \quad (B3)$$

Equation B3 can be reduced to a cubic equation

$$2 \cdot x^3 + x^2 \cdot (x_1^2 + x_2^2 + FO^2) - x_1^2 \cdot x_2^2 \cdot FO^2 = 0, \quad (B4)$$

by multiplying with y^3, where y = 1/x, Equation B4 can be rewritten as

$$-x_1^2 \cdot x_2^2 \cdot FO^2 \cdot y^3 + (x_1^2 + x_2^2 + FO^2) \cdot y + 2 = 0, \quad (B5)$$

Equation B5 has roots defined as

$$\frac{1}{w_{1opt}^2} = \left(\sqrt{\frac{p^3}{27} + \frac{q^2}{4}} - \frac{q}{2} \right)^{\frac{1}{3}} + \left(-\sqrt{\frac{p^3}{27} + \frac{q^2}{4}} - \frac{q}{2} \right)^{\frac{1}{3}}, \quad (B6)$$

where $p = -(x_1^2 + x_2^2 + FO^2)/(x_1^2 \cdot x_2^2 \cdot FO^2)$, and $q = -2/(x_1^2 \cdot x_2^2 \cdot FO^2)$. Equation B6 is known as the Cardano-Tartaglia formula.